Parapierrotite from the Monte Arsiccio mine (Apuan Alps, Tuscany, Italy): occurrence and new data on its crystal-chemistry

Cristian BIAGIONI[1,*], Yves MOËLO[2], Natale PERCHIAZZI[1], Nicola DEMITRI[3] and Federica ZACCARINI[4]

[1]Dipartimento di Scienze della Terra, Università di Pisa, Via S. Maria 53, 56126 Pisa, Italy
*Corresponding author, e-mail: cristian.biagioni@unipi.it
[2]Institut des Matériaux Jean Rouxel, UMR 6502, CNRS, Université de Nantes, 2 rue de la Houssinière,
44322 Nantes Cedex 3, France
[3]Elettra-Sincrotrone Trieste S.C.p.A., S.S. 14 km 163, 5 in Area Science Park, Basovizza, 34149 Trieste, Italy
[4]Department of Applied Geological Sciences and Geophysics, University of Leoben, Peter Tunner Str. 5,
8700 Leoben, Austria

Abstract: A new finding of parapierrotite from the Monte Arsiccio mine, Apuan Alps, Tuscany, Italy, is reported here. Parapierrotite was identified in two different samples, as striated prismatic crystals, black in colour, ranging from 0.05 to 0.5 mm in length. In the studied specimens, parapierrotite is associated with sphalerite, zinkenite, tetrahedrite, and routhierite or with stibnite, protochabournéite, and routhierite. Chemical analysis indicated the presence of a Pb-bearing variety of parapierrotite; the electron microprobe data are (average of 15 spot analyses – in wt%): Tl 17.06(33), Pb 3.64(55), As 0.09(7), Sb 56.07(38), S 23.94(13), total 100.80(34). On the basis of $\Sigma Me = 6$ atoms per formula unit, the chemical formula of Pb-bearing parapierrotite from the Monte Arsiccio mine is $Tl_{0.89(1)}Pb_{0.19(3)}(Sb_{4.91(13)}As_{0.01(1)})_{\Sigma 4.92}S_{7.96(36)}$, ideally $Tl_{0.9}Pb_{0.2}Sb_{4.9}S_8$. Its crystal structure study gave a monoclinic unit cell, space group Pn, with $a = 8.1005(14)$, $b = 19.4385(9)$, $c = 9.0359(4)$ Å, $\beta = 92.041(3)°$, $V = 1421.9(3)$ Å^3, $Z = 4$. The crystal structure was refined to $R_1 = 0.046$ on the basis of 10 461 reflections with $F_o > 4\sigma(F_o)$ and 265 refined parameters. Parapierrotite belongs to the pierrotite–parapierrotite homeotypic pair. The refinement of the crystal structure of this Pb-bearing variety allowed the description of the mechanism favouring the hosting of Pb in one of the two (010) walls of (Tl,Sb) atom pairs of this Tl sulfosalt.

Key-words: parapierrotite; sulfosalt; thallium; antimony; crystal structure; Monte Arsiccio mine; Apuan Alps.

1. Introduction

The occurrence of well-crystallized sulfosalts in the hydrothermal veins from the Apuan Alps Metamorphic Complex (northern Apennines, Italy) has been known since the 19th century (*e.g.*, D'Achiardi, 1873), whereas the mineralogical study performed in the last forty years allowed the descriptions of several very rare sulfosalt species, in some cases characterized by a peculiar crystal-chemistry (*i.e.*, oxysulfosalts, oxychlorosulfosalts, and persulfosalts, *e.g.*, Orlandi *et al.*, 1999, 2001, 2002). Thallium sulfosalts, first described in the Apuan Alps from the Monte Arsiccio mine at the beginning of the 2010s (Orlandi *et al.*, 2012), have to be added to this long list.

The thallium-rich nature of the Monte Arsiccio ore deposit allowed the description of three new thallium sulfosalts (*i.e.*, boscardinite – Orlandi *et al.*, 2012; protochabournéite – Orlandi *et al.*, 2013; arsiccioite – Biagioni *et al.*, 2014b), as well as thallium-bearing varieties of lead sulfosalts, *i.e.*, rouxelite and chovanite (Biagioni *et al.*, 2014c, 2018a; Biagioni & Moëlo, 2017b). Moreover, other

thallium sulfosalts, previously reported from other localities world-wide, have been identified, *i.e.*, routhierite (Biagioni *et al.*, 2014a), chabournéite (Biagioni & Moëlo, 2017a), and parapierrotite.

Parapierrotite is a thallium-antimony sulfosalt having ideal formula $TlSb_5S_8$. It was first described by Johan *et al.* (1975) from Allchar (Macedonia). These authors identified parapierrotite also at Jas Roux (France), where it was later fully described by Johan & Mantienne (2000). On the basis of X-ray diffraction studies, Johan *et al.* (1975) gave the following unit-cell parameters: $a = 8.02(2)$, $b = 19.35(5)$, $c = 9.03(2)$ Å, $\beta = 91.97(8)°$, $V = 1401(9)$ Å^3. The proposed space group was $P2_1/n$. Electron microprobe analyses on crystals from Allchar pointed out the occurrence of Tl, Sb, As, and S, and, in some cases, traces of Pb. Engel (1980) solved the crystal structure of synthetic $TlSb_5S_8$ in the space group Pn, with unit-cell parameters $a = 8.098(5)$, $b = 19.415(12)$, $c = 9.059(6)$ Å, $\beta = 91.96(8)°$, $V = 1423.4(16)$ Å^3. After the first findings at Allchar and Jas Roux, parapierrotite was also identified at the Hemlo gold deposit (Ontario, Canada – Harris, 1989), at the Lookout Pass (Utah,

© 2019 E. Schweizerbart'sche Verlagsbuchhandlung, 70176 Stuttgart, Germany

USA – King & Richardson, 2014), at the Lengenbach quarry (Binn Valley, Switzerland – Raber, 2016), and at the Vorontsovskoe gold deposit (northern Urals, Russia – Plášil *et al.,* 2018). Using a sample from the latter locality, Plášil *et al.* (2018) refined the crystal structure of parapierrotite, confirming the results of Engel (1980). Parapierrotite is monoclinic, space group *Pn*, with unit-cell parameters $a = 8.0832(5)$, $b = 19.4057(11)$, $c = 9.0465(5)$ Å, $\beta = 91.908(6)°$, $V = 1418.25(1)$ Å^3.

The new finding of parapierrotite in the thallium-rich sulfosalt assemblages from the Monte Arsiccio mine (Apuan Alps, Italy) promoted an additional crystal-chemical investigation of this very rare thallium-antimony sulfosalt. Indeed, the Pb-bearing nature of one of the studied samples allowed to investigate the mechanism of incorporation of this element in the crystal structure of parapierrotite.

2. Experimental procedure

2.1. Sample description

Parapierrotite was collected in veins hosted in the metadolostone exposed in the Sant'Olga tunnel, Monte Arsiccio mine, Stazzema, Apuan Alps, Tuscany, Italy (latitude 43° 58′16″N, 10°17′05″E). This mine exploited a pyrite ± baryte ± iron oxide ore-deposit embedded close to the contact between Paleozoic phyllite and Triassic metadolostone. The geological setting of this ore deposit was previously reported by Costagliola *et al.* (1990), whereas new geochemical data can be found in D'Orazio *et al.* (2017) and George *et al.* (2018). In the Sant'Olga tunnel, a decametre-sized lens of metadolostone, locally enriched in pyrite or magnetite, is exposed. The metadolostone shows the occurrence of several vein systems, characterized by a variable and complex mineralogy. Close to the contact between the metadolostone and the pyrite + baryte ore body, a thallium-bearing sulfosalt assemblage has been discovered (Biagioni *et al.*, 2013).

Parapierrotite was identified from two different assemblages. In the first one (hereafter sample #1), parapierrotite occurs as deeply striated prismatic crystals (Fig. 1), up to 50 μm in length, black in colour with a bluish tarnish, associated with stibnite, protochabournéite, and routhierite. In the second occurrence (hereafter sample #2), parapierrotite was observed as striated black prismatic crystals, up to 0.5 mm in length, associated with zinkenite and a member of the tetrahedrite isotypic series (Fig. 2). In the same veins, yellow-orange sphalerite, stibnite, and rare routhierite were observed.

2.2. Chemical data

Quantitative chemical analyses of parapierrotite from the Monte Arsiccio mine were collected on sample #2 using a Superprobe JEOL JXA 8200 electron microprobe (WDS mode, 20 kV, 10 nA, 1 μm beam diameter) at the Eugen F. Stumpfl laboratory, Leoben University. Standards (element, emission line) were: galena (Pb *M*α), lorándite (As *L*α, Tl *M*α), and stibnite (S *K*α, Sb *L*α). Counting times
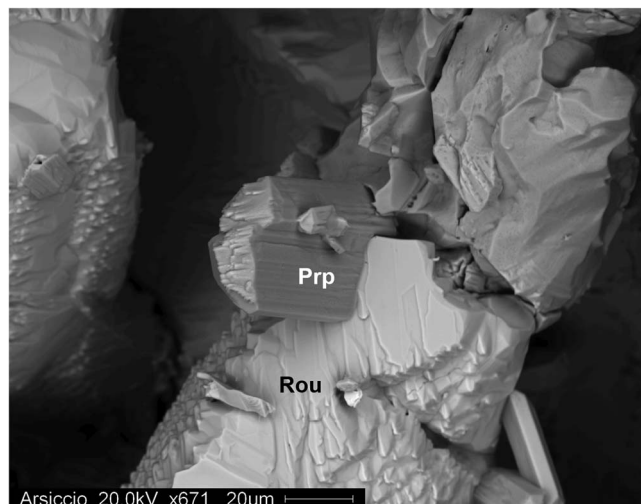

Fig. 1. Parapierrotite (Prp), as black striated prismatic crystal on routhierite (Rou). Sant'Olga level, Monte Arsiccio mine. Sample #1.

were 20 s for peaks and 10 s for left and right backgrounds, respectively. Electron microprobe data for parapierrotite are given in Table 1. On the basis of ΣMe = 6 atoms per formula unit (*apfu*), its chemical formula can be written as $Tl_{0.89}Pb_{0.19}(Sb_{4.91}As_{0.01})_{\Sigma 4.92}S_{7.96}$. After adding Sb and Tl according to the substitutions $2\ Pb^{2+} = Tl^+ + Sb^{3+}$, and subtracting As according to $As^{3+} = Sb^{3+}$, the formula can be written as $Tl_{0.98}Sb_{5.02}S_{7.96}$, in good agreement with the ideal composition $TlSb_5S_8$. Backscattered-electron image and X-ray maps (Fig. 2) show that parapierrotite is chemically homogeneous, and that Tl and Pb are distinctly partitioned between this mineral and associated zinkenite.

Sample #1, represented by a single μm-sized crystal, was only qualitatively analysed using a Phillips XL30 Scanning Electron Microscope equipped with an EDAX DX4 system. The only elements with $Z > 9$ were Tl, Sb, and S. Arsenic and Pb were below the detection limit. This As-free sample corresponds to the natural equivalent of synthetic $TlSb_5S_8$ (Engel, 1980).

2.3. Crystallography

Sample #1 was identified on the basis of single-crystal X-ray diffraction data collected at the XRD1 beamline, ELETTRA synchrotron radiation facility (Lausi *et al.*, 2015). A monochromatic wavelength of 0.59040 Å was used on a 50×50 μm^2 beam size, using a Dectris Pilatus 2M hybrid pixel area detector at a distance of 85 mm. A total of 720 frames was collected using φ scan mode in $\Delta\varphi = 0.5°$ slices, with an exposure time of 2 s. The diffraction data, collected at room temperature, were indexed, integrated, scaled, and corrected for the Lorentz-polarization factor using the software XDS (Kabsch, 2010). The refined unit-cell parameters are $a = 8.087(2)$, $b = 19.407(4)$, $c = 9.056(2)$ Å, $\beta = 91.978(14)°$, $V = 1420.4(6)$ Å^3, space group *Pn*.

Sample #2 was studied collecting single-crystal X-ray diffraction data using a Bruker Smart Breeze diffractometer with an air-cooled CCD detector, with
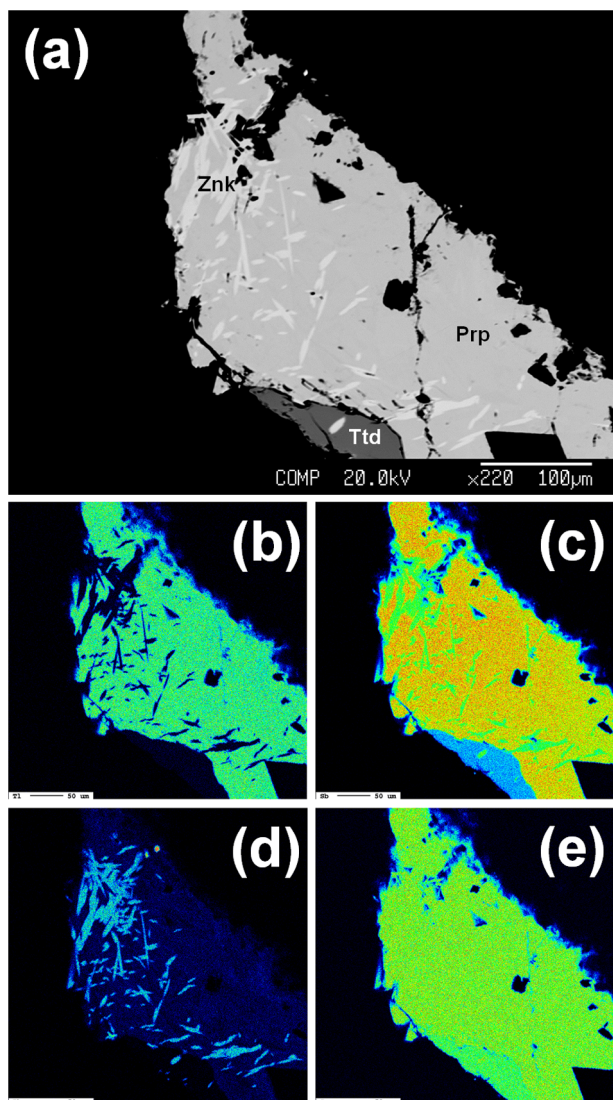
Fig. 2. Backscattered electron image of sample #2 (a) and X-ray maps for Tl (b), Sb (c), Pb (d), and S (e). Labels: Prp = parapierrotite; Ttd = tetrahedrite; Znk = zinkenite.

Table 1. Electron microprobe data of parapierrotite from Monte Arsiccio (sample #2): chemical composition as wt% and chemical formula (in atoms per formula unit, *apfu*) on the basis of $\Sigma Me = 6$ *apfu*.

Element	# 2 ($n = 15$)		
	wt%	Range	e.s.d.
Tl	17.06	16.43–17.64	0.33
Pb	3.64	2.52–4.61	0.55
As	0.09	0.00–0.19	0.07
Sb	56.07	55.48–56.51	0.38
S	23.94	23.72–24.16	0.13
Total	100.80	100.26–101.50	0.34
	apfu	Range	e.s.d.
Tl	0.89	0.86–0.92	0.01
Pb	0.19	0.13–0.24	0.03
As	0.01	0.00–0.03	0.01
Sb	4.91	22.48–22.82	0.13
S	7.96	46.63–47.63	0.36
Ev^*	+0.7	0.0–1.8	0.1
$Tl_{corr.}$**	0.98	0.98–0.99	0.03
$(Sb + As)_{corr.}$**	5.02	5.01–5.02	0.04

*Relative error on the valence equilibrium (%), calculated as $[\Sigma(\text{val} +) - \Sigma(\text{val}-)] \times 100/\Sigma(\text{val}-)$.
**$Tl_{corr.}$ and $(Sb + As)_{corr.}$ on the basis of the substitution $2Pb^{2+} = Tl^+ + (Sb,As)^{3+}$.

Table 2. Crystal data and summary of parameters describing data collection and refinement for parapierrotite (sample #2).

Crystal data	
Crystal size (mm)	$0.28 \times 0.18 \times 0.09$
Cell setting, space group	Monoclinic, Pn
a (Å)	8.1005(14)
b (Å)	19.4385(9)
c (Å)	9.0359(4)
β (°)	92.041(3)
V (Å^3)	1421.9(3)
Z	4
Data collection and refinement	
Radiation, wavelength (Å)	Mo $K\alpha$, $\lambda = 0.71073$
Temperature (K)	293
$2\theta_{max}$	71.06
Measured reflections	41 824
Unique reflections	12 393
Reflections with $F_o > 4\sigma(F_o)$	10 461
R_{int}	0.0439
$R\sigma$	0.0646
Range of h, k, l	$-12 \leq h \leq 12$, $-31 \leq k \leq 31$, $-14 \leq l \leq 14$
R_1 [$F_o > 4\sigma(F_o)$]	0.0462
R (all data)	0.0607
wR (on F_o^2)	0.0881
Goof	1.059
No. of least-squares parameters	265
Maximum and minimum residual peak (e Å^{-3})	2.94 (at 0.74 Å from Tl2a) −1.45 (at 1.70 Å from S2)

graphite-monochromatised Mo $K\alpha$ radiation. The detector-to-crystal distance was set at 50 mm. A total of 2604 frames was collected using ω scan modes in $\Delta\varphi = 0.5°$ slices, with an exposure time of 10 s. Data were corrected for Lorentz-polarization factors and absorption using the package of software *Apex3* (Bruker AXS Inc., 2016). The statistical tests on the distribution of $|E|$ values ($|E^2 - 1| = 0.729$) suggested the absence of a centre of symmetry, whereas the systematic absences agree with the space group Pn. The refined unit-cell parameters are $a = 8.1005(14)$, $b = 19.4385(9)$, $c = 9.0359(4)$ Å, $\beta = 92.041(3)°$, $V = 1421.9(3)$ Å^3.

In both cases, the crystal structure of parapierrotite was refined using *Shelxl*-2018 (Sheldrick, 2015), starting from the atomic coordinates of parapierrotite given by Plášil *et al.* (2018). Scattering curves for neutral atoms were taken from the *International Tables for Crystallography* (Wilson, 1992). Several cycles of isotropic refinement led to $R_1 = 0.096$ and 0.087 for samples #1 and 2, respectively,

confirming the correctness of the structural model. These agreement factor values were lowered to 0.090 and 0.086 taking into account the occurrence of racemic twinning. Assuming an anisotropic model for cations, the R_1 values

dropped to 0.058 and 0.052 for samples #1 and 2, respectively, further lowered to 0.056 and 0.050 introducing the anisotropic displacement parameters also for S atoms. At this stage of the refinements, sample #1 showed relatively high residuals (up to 8.28 $e/Å^3$ at 0.66 Å from Tl2) around cation positions, whereas sample #2 showed two residuals slightly higher than the others and close to Tl2 and Sb9 positions (5.70 $e/Å^3$ at 0.75 Å from Tl2 and 5.69 $e/Å^3$ at 0.69 Å from Sb9. The remaining residual peaks had the highest electron density of 3.40 $e/Å^3$). The addition of these maxima in the refinement of sample #2 revealed the position of two split Pb sites, and lowered the R_1 factor down to 0.046. It should be noted that the U_{eq} value of Tl2 was significantly higher than those of Tl1 before the addition of the two residuals, whereas it was similar to that of Tl1 after this addition. The refined site occupancy factor (s.o.f.) at the two split Tl2A/Pb2B and Sb9A/Pb9B, constrained to full occupancy, indicated the occurrence of 0.09 Pb *apfu* (taking into account the formula unit with $Z = 4$), slightly lower than the Pb content determined through electron-microprobe data. The examination of the difference-Fourier maps revealed that minor Pb could partially occur also at Tl1 (at the split Pb1b site) and Sb3 positions, increasing the total amount of Pb to 0.11 *apfu*. On the contrary, residuals occurring in sample #1 are not related to the occurrence of Pb. The addition of the split position Pb2B resulted in very low s.o.f. [0.02(1)]; moreover, the U_{eq} value of Tl1 and Tl2 in sample #1 are similar and do not suggest any splitting of these positions.

In the following only the structural details of sample #2 are given, allowing the description of the mechanism favouring the hosting of Pb in the crystal structure of parapierrotite. The refinement performed on sample #1 agrees with the structural features previously described by Engel (1980) and Plášil *et al.* (2018). Details of the intensity data collection and crystal-structure refinement for sample #2 are given in Table 2. Crystallographic Information Files for both samples are available as Supplementary Material linked to this article and freely available at https://pubs.geoscience-world.org/eurjmin/.

3. Crystal-structure description

3.1. General organization and cation coordination

Atomic coordinates, site occupancies, and equivalent isotropic displacement parameters of parapierrotite are given in Table 3, whereas selected bond distances and bond-valence sums are shown in Tables 4 and 5, respectively. The unit-cell content of parapierrotite is shown in Fig. 3. It contains 12 independent cation positions (three of them are split) and 16 S sites.

The general organization of parapierrotite, as seen down **c**, is shown in Fig. 4. This mineral is a $N(1,2) = 3,3$ member of the pierrotite homeotypic pair (Moëlo *et al.*, 2008), formed by pierrotite, $Tl_2(Sb,As)_{10}S_{16}$ (Guillemin *et al.*, 1970; Engel *et al.*, 1983) and parapierrotite. The crystal structure of the latter can be described as an alternation,
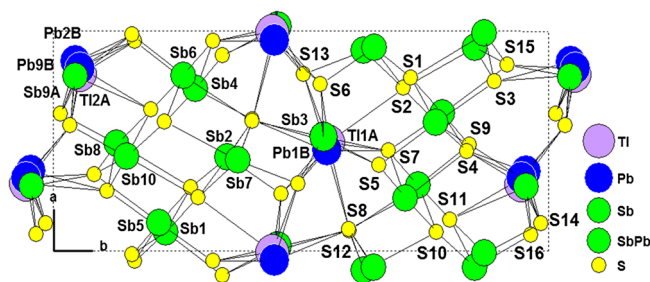

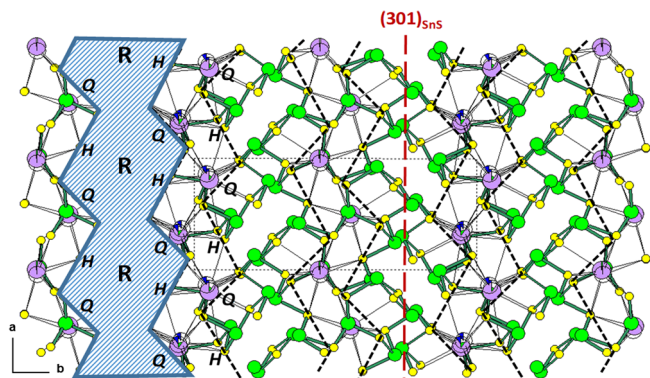Fig. 3. Unit-cell content of parapierrotite, as seen down **c**.

Fig. 4. General organization of parapierrotite, as seen down **c**, according to the rod-layer organization parallel to (010) described by Makovicky (2018). R: rods parallel to [001], stacked along **a** to form one rod-layer (left, blue hatched). Zig–zag lines (blue lines, or black dashed lines): interfaces between rod-layers, with *Q* ribbons [(Tl, Pb) atoms in square coordination with S atoms] in front of *H* ribbons (pseudo-hexagonal nets of S atoms). Short Sb–S bonds (green): d(Sb–S) < 2.72 Å.

along **b**, of unit-cell twinned SnS-like slabs separated by zig-zag walls composed of columns of (Tl,Pb) and (Sb, Pb)-centred "standing" trigonal prisms. Compared to a [010] projection of SnS structure (Del Bucchia *et al.*, 1981), each slab is close to a cut-off along $(301)_{SnS}$, three hemi-octahedra large.

A careful description of the structural arrangement of parapierrotite has recently been given by Makovicky (2018). According to this author, slabs can be described as rod-layers, connected along **b** through a *H/Q* interface (Fig. 4).

Cation distribution in the layer interface is detailed in Fig. 5. Thallium is hosted at the Tl1A and Tl2A sites. The former has a tricapped trigonal prismatic coordination, with average bond distance of 3.388 Å; the latter has a trigonal prismatic coordination, with a capping ligand and two additional long bonds on the same side of the prism, at 3.75 and 3.82 Å. Its average bond distance is 3.357 Å. The coordination of Tl2A is similar to the bicapped trigonal prisms occupied by Pb in the crystal structure of lillianite homologues (Makovicky, 2018). Bond-valence sums at Tl1A and Tl2A, assuming their full-occupancy, are 1.00 and

Table 3. Atomic coordinates, site occupation factors (s.o.f.), and equivalent isotropic displacement parameters ($Å^2$) for parapierrotite.

Site	s.o.f.	x	y	z	U_{eq}
Tl1A	$Tl_{0.98(1)}$	−0.00443(12)	0.44278(3)	−0.00215(12)	0.0314(2)
Pb1B	$Pb_{0.02(1)}$	−0.046(5)	0.4456(15)	−0.052(5)	0.0314(2)
Tl2A	$Tl_{0.91(1)}$	−0.19628(15)	0.05391(4)	0.73581(8)	0.0332(2)
Pb2B	$Pb_{0.09(1)}$	−0.1345(17)	0.0440(5)	0.7213(10)	0.0332(2)
Sb1	$Sb_{1.00}$	0.08549(10)	0.22712(5)	0.28779(9)	0.02187(16)
Sb2	$Sb_{1.00}$	0.42494(9)	0.35152(4)	0.25919(9)	0.01721(14)
Sb3	$Sb_{0.98(1)}Pb_{0.02(1)}$	0.01989(11)	0.45302(5)	0.44731(10)	0.0264(2)
Sb4	$Sb_{1.00}$	−0.26185(9)	0.28770(4)	0.54169(8)	0.01682(14)
Sb5	$Sb_{1.00}$	0.12732(9)	0.21366(4)	0.73057(8)	0.01818(15)
Sb6	$Sb_{1.00}$	−0.20124(10)	0.26217(4)	0.98335(8)	0.01806(14)
Sb7	$Sb_{1.00}$	−0.58775(9)	0.37225(4)	0.78527(8)	0.01677(14)
Sb8	$Sb_{1.00}$	0.49009(10)	0.12843(4)	0.46653(8)	0.01858(15)
Sb9A	$Sb_{0.91(1)}$	0.79351(19)	0.04422(7)	0.20011(15)	0.0203(2)
Pb9B	$Pb_{0.09(1)}$	0.8324(11)	0.0545(5)	0.2206(11)	0.0203(2)
Sb10	$Sb_{1.00}$	0.42671(10)	0.14825(4)	0.02603(10)	0.02266(16)
S1	$S_{1.00}$	0.2878(4)	0.27738(15)	0.4623(3)	0.0176(5)
S2	$S_{1.00}$	0.2421(4)	0.29244(15)	0.0788(3)	0.0175(5)
S3	$S_{1.00}$	0.2716(3)	0.10888(14)	0.2739(3)	0.0158(5)
S4	$S_{1.00}$	−0.0464(3)	0.16469(15)	0.5345(3)	0.0168(5)
S5	$S_{1.00}$	−0.1111(3)	0.34167(14)	0.3277(3)	0.0154(5)
S6	$S_{1.00}$	0.2597(4)	0.45976(15)	0.2806(4)	0.0218(6)
S7	$S_{1.00}$	−0.0464(3)	0.32239(14)	0.7301(3)	0.0153(5)
S8	$S_{1.00}$	−0.4009(4)	0.40187(14)	0.5850(3)	0.0176(5)
S9	$S_{1.00}$	−0.0165(4)	0.15924(14)	0.9449(3)	0.0169(5)
S10	$S_{1.00}$	−0.4121(4)	0.22494(17)	0.8065(3)	0.0205(6)
S11	$S_{1.00}$	−0.3574(4)	0.19764(16)	0.1929(3)	0.0190(5)
S12	$S_{1.00}$	−0.4068(4)	0.40122(16)	0.9956(3)	0.0207(6)
S13	$S_{1.00}$	−0.6954(4)	0.49366(15)	0.7811(3)	0.0194(5)
S14	$S_{1.00}$	0.6240(4)	0.01476(16)	0.4161(4)	0.0233(6)
S15	$S_{1.00}$	0.3471(4)	0.08285(15)	0.6867(3)	0.0204(5)
S16	$S_{1.00}$	0.5736(4)	0.03438(16)	0.0107(4)	0.0238(6)

Table 4. Selected bond-distances (in Å) in parapierrotite.

Tl1A			Pb1B			Tl2A			Pb2B			Sb1		
	−S8	3.224(3)		−S6	2.83(5)		−S4	3.095(3)		−S14	2.920(12)		−S1	2.438(3)
	−S13	3.279(3)		−S12	3.10(4)		−S9	3.112(3)		−S4	2.991(9)		−S2	2.638(3)
	−S6	3.290(4)		−S7	3.10(3)		−S16	3.181(4)		−S16	3.002(14)		−S3	2.754(3)
	−S6	3.291(3)		−S13	3.39(3)		−S3	3.195(3)		−S3	3.109(10)		−S5	2.769(3)
	−S12	3.358(3)		−S8	3.40(3)		−S14	3.278(3)		−S9	3.142(10)		−S4	2.782(3)
	−S7	3.374(3)		−S13	3.49(4)		−S14	3.296(4)		−S14	3.372(10)		−S9	3.441(3)
	−S13	3.381(3)		−S6	3.83(5)		−S16	3.490(4)		−S16	3.593(13)		−S11	3.704(3)
	−S2	3.600(3)					−S15	3.746(4)						
	−S5	3.698(3)					−S10	3.821(4)						
Sb2	−S2	2.449(3)	Sb3	−S13	2.487(3)	Sb4	−S7	2.488(3)	Sb5	−S4	2.418(3)	Sb6	−S10	2.409(3)
	−S6	2.505(3)		−S6	2.504(3)		−S8	2.525(3)		−S9	2.527(3)		−S9	2.530(3)
	−S1	2.612(3)		−S5	2.626(3)		−S5	2.549(3)		−S7	2.539(3)		−S11	2.632(3)
	−S12	2.949(3)		−S12	2.924(4)		−S4	2.962(3)		−S1	3.054(3)		−S7	2.896(3)
	−S8	3.364(3)		−S7	3.656(3)		−S10	2.984(3)		−S15	3.137(3)		−S12	3.179(3)
	−S11	3.534(4)		−S8	3.802(3)		−S11	3.664(3)		−S2	3.592(3)		−S5	3.527(3)
	−S5	3.792(3)		−S13	3.814(3)		−S1	3.698(3)		−S10	3.776(3)		−S2	3.710(3)
Sb7	−S12	2.424(3)	Sb8	−S3	2.467(3)	Sb9A	−S16	2.433(4)	Pb9B	−S14	2.604(10)	Sb10	−S11	2.463(3)
	−S8	2.469(3)		−S15	2.499(3)		−S14	2.492(3)		−S15	2.691(10)		−S16	2.519(3)
	−S13	2.516(3)		−S14	2.510(3)		−S15	2.512(3)		−S16	2.804(10)		−S3	2.717(3)
	−S10	3.200(3)		−S11	3.109(3)		−S11	3.223(3)		−S11	3.184(10)		−S10	2.837(3)
	−S2	3.406(3)		−S1	3.326(3)		−S9	3.597(3)		−S9	3.474(10)		−S2	3.220(3)
	−S1	3.567(3)		−S10	3.662(3)		−S16	3.861(4)		−S16	3.648(10)		−S15	3.361(3)
	−S7	3.854(3)		−S4	3.848(3)					−S4	3.660(10)		−S9	3.645(3)
										−S3	3.726(10)			

Table 5. Bond-valence balance (in valence unit, v.u.) for parapierrotite.

Site	S1	S2	S3	S4	S5	S6	S7	S8	S9	S10	S11	S12	S13	S14	S15	S16	Σ cations	Theor.
Tl1A		0.06			0.04	0.13	0.11	0.16				0.11	0.14				0.98	0.98
						0.13							0.10					
Pb1B						0.01	–	–				–	–				0.01	0.02
Tl2A			0.16	0.21					0.20	0.03				0.13	0.04	0.17	1.13	0.91
														0.12		0.07		
Pb2B			0.02	0.03					0.02					0.03		0.03	0.15	0.18
														0.01		0.01		
Sb1	1.03	0.60	0.44	0.41	0.42				0.07		0.03						3.00	3.00
Sb2	0.65	1.00			0.03	0.86		0.08			0.05	0.26					2.93	3.00
Sb3					0.63	0.87	0.04	0.03				0.28	0.91				2.79	2.98
													0.03					
Sb4	0.03			0.25	0.77		0.90	0.82		0.24	0.04						3.05	3.00
Sb5	0.20	0.05		1.09			0.79		0.81	0.03					0.16		3.13	3.00
Sb6		0.03			0.05		0.30		0.81	1.12	0.61	0.14					3.06	3.00
Sb7	0.05	0.08					0.02	0.95		0.13		1.07	0.84				3.14	3.00
Sb8	0.09		0.96	0.02						0.04	0.17			0.85	0.88		3.01	3.00
Sb9A									0.04		0.11			0.81	0.77	0.95	2.70	2.73
																0.02		
Pb9B			–	–					0.01		0.02			0.08	0.06	0.05	0.22	0.18
Sb10		0.12	0.49						0.04	0.35	0.97				0.09	0.83	2.89	3.00
Σ anions	2.05	1.94	2.07	2.01	1.94	2.00	2.16	2.04	2.00	1.94	2.00	1.86	2.02	2.03	2.00	2.13		

Note: bond-valence parameters after Brese & O'Keeffe (1991) were used for Pb–S and Sb–S bonds. The value proposed by Biagioni *et al.* (2014b) was used for Tl–S bonds.

1.23 valence unit (v.u.), respectively. The slight overbonding at Tl2A could indicate the occurrence of minor Pb at this site. In addition, minor Pb is hosted at the split positions Pb1B and Pb2B, having a seven-fold coordination. Whereas Pb2B has a typical monocapped trigonal prismatic coordination, with average bond distance of 3.161 Å, the coordination of Pb1B is less defined, likely owing to the very low site occupancy (only 0.02 *apfu*), not allowing the resolution of the actual ligand positions. The split pairs Tl1A/Pb1B and Tl2A/Pb2B alternate, along **c**, with the mixed (Sb,Pb) site Sb3 and the split pair Sb9A/Pb9B, respectively. Sb3 has the typical trigonal pyramidal coordination of Sb atoms, with three short Sb–S distances (average distance = 2.539 Å). The short Sb–S bonds are oriented along $[00\bar{1}]$, giving a polar character to the Tl1/Sb3 columns (Fig. 5). In agreement with the refined s.o.f., minor Pb replaces Sb at this position, being related to the (Tl:Pb) atomic ratio at the split pair Tl1A/Pb1B. Sb9A has three short bonds, with average Sb–S distance of 2.479 Å. In this column, the short bonds are oriented toward the PbS-like slabs and connect along **c** successive Tl2A/Pb2B sites thought sharing the S14 and S16 sites (Fig. 5). The split Pb9B has a distorted bicapped trigonal prismatic coordination, with average Pb–S distance of 3.224 Å.

The PbS-like slab is formed by pure Sb sites. Sites Sb2, Sb4, Sb6, Sb7, and Sb8 have a typical trigonal pyramidal coordination, with average bond distances ranging from 2.470 (Sb7) to 2.524 Å (Sb6). Sb1 and Sb10 have only two bonds shorter than 2.70 Å. Actually, the latter has the third bond at 2.717 Å, and a fourth one at 2.837 Å, whereas the former has three bonds between 2.754 and 2.782 Å. Bond-valence sums range between 2.89 (Sb10) and 3.14 v.u. (Sb7).

3.2. Modular analysis according to the polymerization of short Sb–S bonds

Complementary to the rod-layer representation of Makovicky (2018), another description can be proposed enhancing shortest (*i.e.*, strongest) Sb–S bonds. Selecting the cut-off distance of 2.72 Å (a little bit longer than the value of 2.70 Å of Moëlo *et al.*, 2012), SbS₃ trigonal pyramidal polyhedra can be revealed for all Sb positions, except Sb1 and Sb10. On this basis, the projection of the structure along $[\bar{1}01]$ reveals undulating, two-atom-thick layers (Fig. 6), separated by weak Sb–S bonding, as indicated by Plášil *et al.* (2018). Thus, the (101) plane may act as a cleavage plane.

Suppression of Sb3 and Sb9A, together with Tl1 and Tl2, delimits the constitutive (010) PbS-like slab. Each slab corresponds to the oblique stacking along [101] of Sb_8S_{16} ribbons (Fig. 7, left). The ribbon elongation corresponds to $[210]_{PbS}$ (Fig. 7, right). Projection along [101] of a single undulating layer (Fig. 8) shows that, within a ribbon, the Sb_8S_{16} group is divided into a Sb_6S_{13} distorted chain and a Sb_2S_3 dimer (with Sb1 and Sb2). Taking into account Sb3 and Sb9A, one sees that (i) Sb3 connects the chain and the dimer, and (ii) each Sb_8S_{16} group is connected to four Sb_8S_{16} groups of the neighbouring ribbons (two through Sb3, two others through Sb9A). Thus, there is a complete two-dimensional Sb–S polymerization within an undulating layer. Moreover, Sb1, with only two short Sb–S bonds, shows three medium Sb–S bonds, ranging between 2.72 and 2.80 Å. It corresponds very likely to a mean position, with a possible connection between two Sb_8S_{16} groups within a ribbon through the Sb1–S3 bond.
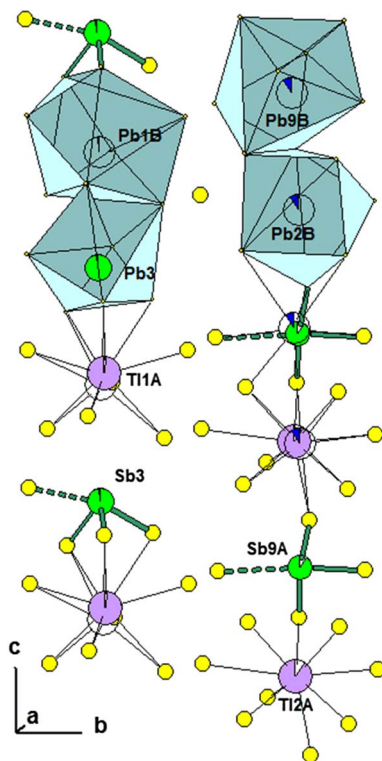
Fig. 5. Cation columns on the zig–zag walls separating PbS-like slabs. Some cations have been omitted, to emphasize Sb and Tl coordination, as well as polyhedra around Pb atoms. Sb–S short and medium bonds: green solid and dashed lines, respectively.
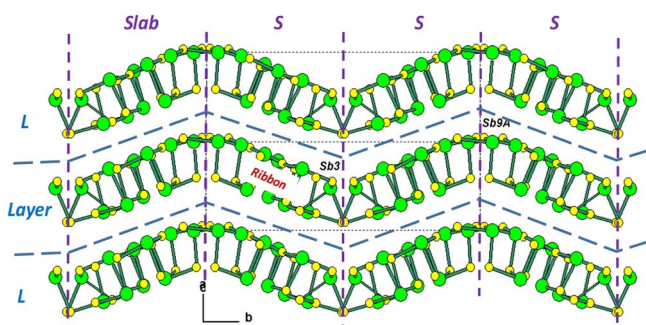

Fig. 6. Undulating layers (L) according to polymerization of short Sb–S bonds (green lines), as seen down $[\bar{1}01]$. Tl and Pb positions have been omitted. Sb3 and Sb9A: Sb atoms alternating with Tl atoms on the walls separating PbS-like slabs (S). Each slab shows the stacking along [101] of two-atom-thick ribbons of Sb with S in triangular pyramidal coordination (Fig. 7).

4. Discussion

4.1. Crystal-chemistry of parapierrotite

The crystal-chemical formula of parapierrotite, as obtained through the refinement of the crystal structure of sample #2, is $(Tl_{1.89}Pb_{0.11})_{\Sigma 2}(Sb_{1.89}Pb_{0.11})_{\Sigma 2}Sb_8S_{16}$ $(Z = 2)$ = $Tl_{0.945}$ $Pb_{0.11}Sb_{4.945}S_8$ $(Z = 4)$, in agreement with electron-microprobe data, i.e., $Tl_{0.89}Pb_{0.19}(Sb_{4.91}As_{0.01})_{\Sigma 4.92}S_{7.96}$.

Although parapierrotite does not strictly belong to the sartorite homologous series, contrary to pierrotite (Makovicky, 2018), one can use the general formula of sartorite homologues, $Me_x^+Me_{4N-8-2x}^{2+}Me_{8+x}^{3+}S_{4N+4}$, first proposed by Makovicky (1985), for describing its crystal-chemical features. This formula, for the ~9 Å periodicity along the columns of trigonal prisms, becomes $Me_x^+Me_{8N-16-2x}^{2+}$ $Me_{16+x}^{3+}S_{8N+8}$, where Me^+ = Tl, Me^{2+} = Pb, and Me^{3+} = ; (Sb, As). In ideal parapierrotite, $x = 4$ and $N = 3$, i.e., $Tl_4Sb_{20}S_{32}$ $(Z = 1)$. Taking into account the electron microprobe data of sample #2 $(4 \times Tl_{0.89}Pb_{0.19}(Sb_{4.91}As_{0.01})_{\Sigma 4.92}$ $S_{7.96} = Tl_{3.56}Pb_{0.76}(Sb_{19.64}As_{0.04})_{\Sigma=19.68}S_{31.84})$, and following the calculation procedures suggested by Makovicky & Topa (2015), the homologue order $N = 2.98$ can be obtained, in perfect agreement with the ideal value. The substitution percentage of Tl is 91%.

The sample #2 from Monte Arsiccio is the richest in Pb so far found. Indeed, lead was not reported in significant amount in any of the available chemical analyses of parapierrotite (Johan et al., 1975; Harris, 1989; Johan & Mantienne, 2000; Plášil et al., 2018). The Pb-to-Tl substitution occurs on the zig–zag walls separating PbS-like slabs, and is coupled with a Pb-to-Sb substitution in the same columns. There is a strong preference of Pb for the Tl2 position, possibly following the similar coordination environment shown by Tl2 with Pb sites occurring in the composition planes of lillianite homologues (Makovicky, 2018). This is also related to the different orientations of the pyramidal coordination of Sb3 and Sb9A, alternating with Tl1 and Tl2, respectively. As indicated by Makovicky (2018), the triangular basis of $Sb3S_3$ pyramid is sub-perpendicular to **c**, while it is sub-parallel for $Sb9AS_3$ pyramid. As a consequence, the $Sb3S_3$ pyramid is connected only with one Tl1 polyhedron, sharing S5, S6, and S13 atoms, with a short Sb3–Tl1 distance (4.06 Å) and a longer one (4.99 Å). Inversely, the $Sb9AS_3$ pyramid is connected with two neighbouring Tl2 polyhedra, through sharing S14 and S16 atoms, with two closer Sb9A–Tl2 distances (4.20 and 4.84 Å). Thus, the shortest connection between Tl2 polyhedra appears as the steric factor that favours Pb substitution. In the isotypic compound KSb_5S_8 (Berlepsch et al., 1999), the same dissymmetry of the lengths of Sb–K distances is observed, i.e., 4.12 and 4.97 Å against 4.26 and 4.81 Å, respectively.

Another interesting chemical feature is the virtually As-free nature of sample #2. Indeed, As was usually reported in the other occurrences, with the highest values measured from Allchar (up to 5.3 wt% As) and Jas Roux (12.5 wt%). The occurrence of As results in a significant contraction of the unit-cell volume, as shown in Table 6 ($\Delta V = \sim -1.6\%$ for the sample from Allchar with respect to synthetic $TlSb_5S_8$).

4.2. Parapierrotite in the framework of the sulfosalt assemblages from the Monte Arsiccio mine

The ore assemblages discovered in the metadolostone lens exposed in the Sant'Olga tunnel, Monte Arsiccio mine, allowed the identification of 24 different sulfosalt species (Table 7). In agreement with Biagioni et al. (2014c), three different kinds of sulfosalt occurrences have been observed:
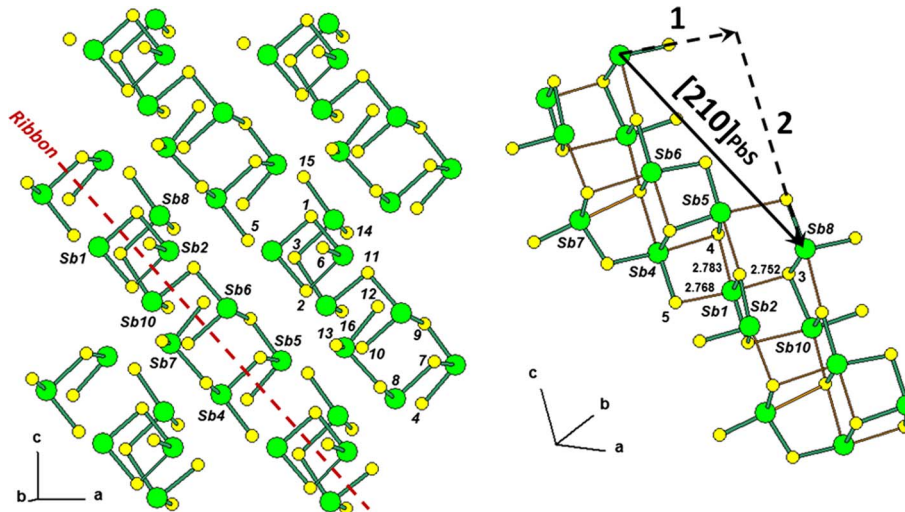
Fig. 7. Left: single slab corresponding to the stacking along **c** of inclined Sb_8S_{16} ribbons. Right: detail of one ribbon showing its orientation according to $[210]_{PbS}$. Weak Sb–S bonds (yellow): d(Sb–S) > 2.72 Å. Medium Sb–S distances around Sb1 (with S3, S4 and S5) have been indicated.
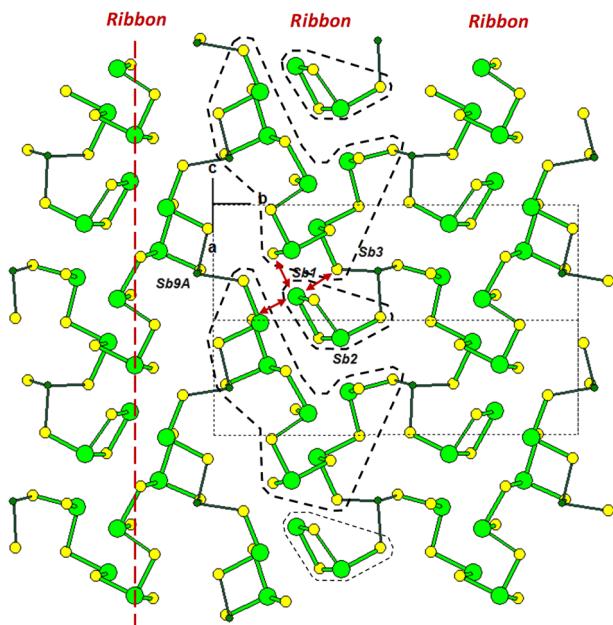

Fig. 8. Projection along [101] of one undulating layer. Black dashed lines circle the Sb_6S_{13} distorted chain and the Sb_2S_3 dimer. Sb3 and Sb9A: Small black atoms at the ribbon interfaces, with black Sb–S bonds. Red double arrows: medium distances around Sb1 (Fig. 7, right).

type (1) = microcrystalline baryte + pyrite; type (2) = pyrite-rich metadolostone; and type (3) = carbonate + baryte + quartz veins embedded in pyrite-poor metadolostone. Sulfosalt assemblages vary as a function of the kind of occurrence.

Thallium sulfosalts are mainly confined to occurrences (1) and (2), whereas in occurrence (3) thallium is a minor component of lead-antimony sulfosalts, *e.g.*, in rouxelite (up to 0.91 Tl *apfu*) and chovanite (up to 0.87 Tl *apfu*)

(Biagioni *et al.*, 2014c, 2018a; Biagioni & Moëlo, 2017b). Only in some cases, carbonate + baryte + quartz veins hosting a thallium-rich sulfosalt assemblage were observed, close to the contact between the microcrystalline baryte + pyrite ore body and the metadolostone lens. Sample #2 was collected in one of these veins, in close association with yellow sphalerite, acicular zinkenite, tetrahedrite, and minor routhierite. However, as stated above, thallium sulfosalts usually occur as interstitial grains in the microcrystalline baryte and pyrite [type (1) occurrence] or as compact masses or veinlets within pyrite-rich metadolostone [type (2) occurrence]. In the latter kind of occurrence, extremely rare and small vugs were observed, where sample #1 of parapierrotite was found, associated with stibnite, routhierite, and protochabournéite. In the same vugs, miargyrite, realgar, baryte, senarmontite, and hörnesite were identified.

Previous studies showed the control of the hosting lithology on the crystal-chemistry of sulfosalts. In the routhierite–arsiccioite isotypic pair, there is a continuous increase in the Ag/(Ag + Cu) and As/(As + Sb) atomic ratios (from 0.202 to 0.869 and from 0.693 to 0.788, respectively) passing from type (3) to type (1) occurrence (Biagioni *et al.*, 2014b). Similarly, boscardinite is progressively enriched in Tl and As from type (3) to type (1) occurrence (Biagioni & Moëlo, 2017a). Additionally, it is worth noting that, whereas protochabournéite was first found in type (3) occurrence, the recently identified chabournéite was collected in a pyrite-rich lithology. Figure 9 shows the relation between As/(As + Sb) and Pb/(Pb + 2Tl) atomic ratios for selected lead-antimony sulfosalts from Monte Arsiccio. Lead-sulfosalts (zinkenite, robinsonite, chovanite, and rouxelite) are the Pb-richest phases, with only minor substitutions of Pb^{2+} by Tl^+ and Sb^{3+} by As^{3+}. Indeed, these phases are hosted in type (3) occurrence, *i.e.*, in veins hosted in pyrite-poor metadolostone. The increasing amount of pyrite in the country rocks favours higher As/(As + Sb) and lower Pb/(Pb + 2Tl) atomic ratios, leading to the

Table 6. Chemical composition and unit-cell parameters in previous studies of parapierrotite and synthetic analogues.

	Chemical formula	a (Å)	b (Å)	c (Å)	β (°)	V (Å^3)	Ref
Synthetic	$TlSb_5S_8$	8.098	19.415	9.059	91.96	1423.4	[1]
Allchar	$Tl_{0.99}(Sb_{4.36}As_{0.64})S_{8.01}$	8.02	19.35	9.03	91.97	1400.5	[2]
Vorontsovskoe	$Tl_{1.01}(Sb_{4.75}As_{0.28})S_{7.95}$	8.083	19.406	9.046	91.91	1418.2	[3]
MA #2	$Tl_{0.91}Pb_{0.18}Sb_{4.91}S_8$	8.100	19.438	9.036	92.04	1421.9	[4]

[1]: Engel (1980); [2]: Johan *et al.* (1975); [3]: Plášil *et al.* (2018); [4]: this work.

Table 7. Sulfosalts identified in the Monte Arsiccio ore deposit.

| Mineral	Chemical formula	Mineral	Chemical formula
Aktashite	$Cu_6Hg_3As_4S_{12}$	Owyheeite	$Ag_3Pb_{10}Sb_{11}S_{28}$
Andreadiniite	$CuAg_7HgPb_7Sb_{24}S_{48}$	Parapierrotite	$TlSb_5S_8$
Arsiccioite	$AgHg_2TlAs_2S_6$	Plagionite	$Pb_5Sb_8S_{17}$
Boscardinite	$Ag_{0.5}TlPb_3Sb_{7.5}As_2S_{18}$	Protochabournéite	$Tl_2Pb(Sb_{9-8}As_{1-2})S_{17}$
Boulangerite	$Pb_5Sb_4S_{11}$	Quatrandorite	$Ag_{7.5}Pb_9Sb_{23.5}S_{48}$
Bournonite	$CuPbSbS_3$	Robinsonite	$Pb_4Sb_6S_{13}$
Chabournéite	$Tl_2Pb(Sb,As)_{10}S_{17}$	Routhierite	$CuHg_2TlAs_2S_6$
Chovanite	$Pb_{28}Sb_{30}S_{72}O$	Rouxelite	$Cu_2HgPb_{22}Sb_{28}S_{64}(O,S)_2$
Ferdowsiite	$Ag_8Sb_5As_3S_{16}$	Senandorite	$AgPbSb_3S_6$
Jamesonite	$FePb_4Sb_6S_{14}$	Tetrahedrite	$Cu_6[Cu_4(Hg,Zn)_2]Sb_4S_{13}$
Laffittite	$AgHgAsS_3$	Twinnite	$Pb(Sb_{0.63}As_{0.37})_2S_4$
Miargyrite	$AgSbS_2$	Zinkenite	$Pb_9Sb_{22}S_{42}$
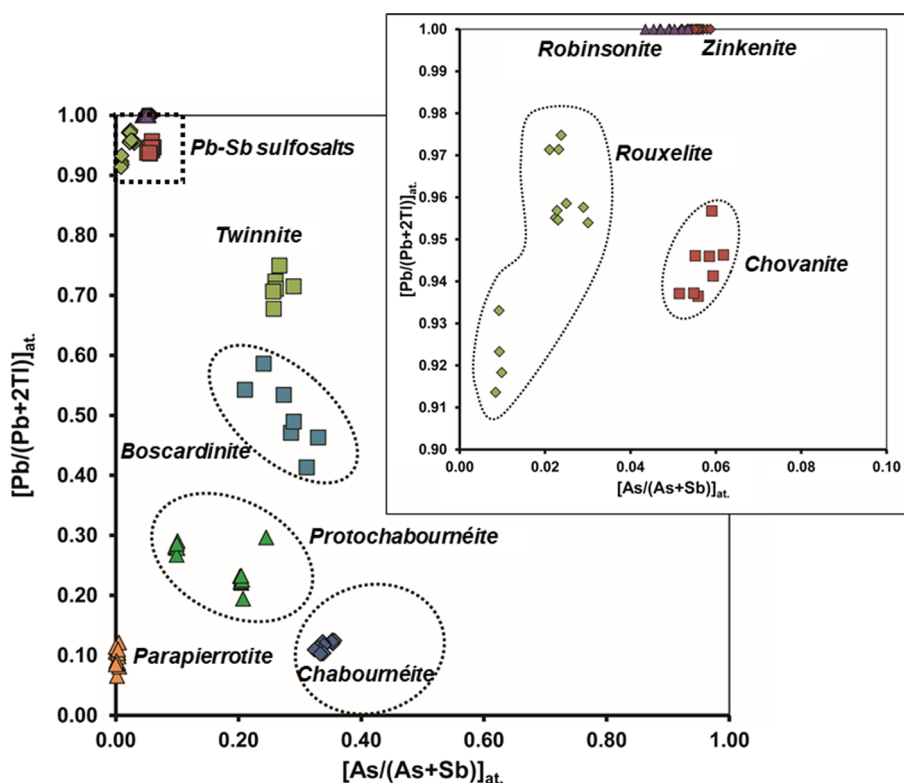
Fig. 9. Pb/(Pb + 2Tl) *versus* As/(As + Sb) atomic ratio in selected sulfosalts from the Monte Arsiccio mine.

widespread crystallization of Tl sulfosalts, showing variable As contents. As stated above, taking into account boscardinite and protochabournéite, higher As/(As + Sb) ratios have been observed passing from type (3) to type (1) occurrence. In the protochabournéite–chabournéite homeotypic pair, chabournéite from Monte Arsiccio is the lowest in

As so far reported world-wide (in Fig. 9 the circle indicates the known chemical variability of this mineral) and was found in veins embedded in a pyrite-rich metadolostone.

Such a relation between the amount of pyrite in the host rocks and the As/(As + Sb) atomic ratio in sulfosalts was qualitatively discussed by Biagioni *et al.* (2016) for the jordanite–geocronite isotypic pair from the Pollone mine. Indeed, availability of Sb in the late stage of sulfosalt crystallization is a common character of almost all the ore deposits in the Apuan Alps, as proved, for instance, by the discovery of protochabournéite, an Sb-rich homeotype of chabournéite (Orlandi *et al.*, 2013), and boscardinite, a Tl–Sb homeotype of baumhauerite (Orlandi *et al.*, 2012). Biagioni *et al.* (2016) proposed that the unusual As-rich composition of sulfosalts from the pyrite-rich environments could be due to the occurrence of a relatively high $f(S_2)$ that may promote the sulfidation of arsenic, acting as an anion in As-bearing pyrite and arsenopyrite, to As^{3+}, during pyrite recrystallization. This agrees with the results of a LA-ICP-MS investigation performed on pyrite from the Monte Arsiccio ore deposit, showing a loss of As, Sb, Tl, Hg, Cu, Zn, Ag, and Mn during the metamorphic recrystallization (George *et al.*, 2018).

Parapierrotite (sample #2) is the Tl-richest and one of the As-poorest sulfosalt from Monte Arsiccio. Its presence in type (3) occurrence agrees with the very low content of As, whereas the unusually high Pb content is in agreement with the Pb-enrichment shown by sulfosalt hosted in the metadolostone. Likely, the occurrence of the As-rich homeotype pierrotite could be possible in pyrite-rich occurrences from Monte Arsiccio.

5. Conclusion

Parapierrotite is the last addition to the thallium sulfosalts reported from the Monte Arsiccio mine. Its peculiar Pb-bearing chemistry agrees with the very complex ore geochemistry of this locality, where Tl-bearing varieties of Pb–Sb sulfosalts were reported (*e.g.*, rouxelite – Biagioni *et al.*, 2014c; chovanite – Biagioni & Moëlo, 2017b, Biagioni *et al.*, 2018a; andreadiniite – Biagioni *et al.*, 2018b). Similarly, Tl sulfosalts are enriched in Pb. For instance, protochabournéite is Pb-enriched with respect to chabournéite and this trend is confirmed by parapierrotite, that is the Pb-richest so far reported world-wide.

Crystal-chemical analysis of Pb-rich parapierrotite has revealed the preferential substitution of Pb on one of the two Sb-Tl pairs (*i.e.*, Sb9A-Tl2), that can be explained by steric reasons, as indicated by the distinct orientations of the two SbS$_3$ triangular pyramids. A possible way to favour the substitution of the other Sb3–Tl1 pair could be the replacement of Pb^{2+} by another divalent cation with a larger ionic radius (*e.g.*, Ba^{2+}).

References

Berlepsch, P., Miletich, R., Armbruster, T. (1999): The crystal structure of synthetic KSb$_5$S$_8$ and (Tl$_{0.598}$K$_{0.402}$)Sb$_5$S$_8$ and their relation to parapierrotite (TlSb$_5$S$_8$). *Z. Kristallogr.*, **214**, 57–63.

Biagioni, C. & Moëlo, Y. (2017a): Lead-antimony sulfosalts from Tuscany (Italy). XVIII. New data on the crystal-chemistry of boscardinite. *Mineral. Mag.*, **81**, 47–60.

—, — (2017b): Lead-antimony sulfosalts from Tuscany (Italy). XIX. Crystal chemistry of chovanite from two new occurrences in the Apuan Alps and its 8 Å crystal structure. *Mineral. Mag.*, **81**, 811–831.

Biagioni, C., D'Orazio, M., Vezzoni, S., Dini, A., Orlandi, P. (2013): Mobilization of Tl-Hg-As-Sb-(Ag,Cu)-Pb sulfosalt melts during low-grade metamorphism in the Alpi Apuane (Tuscany, Italy). *Geology*, **41**, 747–750.

Biagioni, C., Bonaccorsi, E., Moëlo, Y., Orlandi, P. (2014a): Mercury-arsenic sulfosalts from the Apuan Alps (Tuscany, Italy). I. Routhierite, (Cu$_{0.8}$Ag$_{0.2}$)Hg$_2$Tl(As$_{1.4}$Sb$_{0.6}$)$_{\Sigma=2}$S$_6$, from Monte Arsiccio mine: occurrence and crystal structure. *Eur. J. Mineral.*, **26**, 163–170.

Biagioni, C., Bonaccorsi, E., Moëlo, Y., Orlandi, P., Bindi, L., D'Orazio, M., Vezzoni, S. (2014b): Mercury-arsenic sulfosalts from the Apuan Alps (Tuscany, Italy). II. Arsiccioite, AgHg$_2$TlAs$_2$S$_6$, a new mineral from the Monte Arsiccio mine: occurrence, crystal structure and crystal chemistry of the routhierite isotypic series. *Mineral. Mag.*, **78**, 101–117.

Biagioni, C., Moëlo, Y., Orlandi, P. (2014c): Lead-antimony sulfosalts from Tuscany (Italy). XV. (Tl-Ag)-bearing rouxelite from Monte Arsiccio mine: occurrence and crystal chemistry. *Mineral. Mag.*, **78**, 651–661.

Biagioni, C., Dini, A., Orlandi, P., Moëlo, Y., Pasero, M., Zaccarini, F. (2016): Lead-antimony sulfosalts from Tuscany (Italy). XX. Members of the jordanite-geocronite series from the Pollone mine, Valdicastello Carducci: occurrence and crystal structure. *Minerals*, **6**, 15.

Biagioni, C., Moëlo, Y., Perchiazzi, N., Demitri, N., Lepore, G.O. (2018a): Lead-antimony sulfosalts from Tuscany (Italy). XXIV. Crystal structure of thallium-bearing chovanite, TlPb$_{26}$(Sb, As)$_{31}$S$_{72}$O, from the Monte Arsiccio mine, Apuan Alps. *Minerals*, **8**, 535.

Biagioni, C., Moëlo, Y., Orlandi, P., Paar, W.H. (2018b): Lead-antimony sulfosalts from Tuscany (Italy). XXIII. Andreadiniite, CuAg$_7$HgPb$_7$Sb$_{24}$S$_{48}$, a new oversubstituted (Cu,Hg)-rich member of the andorite homeotypic series from the Monte Arsiccio mine, Apuan Alps. *Eur. J. Mineral.*, **30**, 1021–1035.

Brese, N.E. & O'Keeffe, M. (1991): Bond-valence parameters for solids. *Acta Crystallogr.*, **B47**, 192–197.

Bruker AXS Inc. (2016): APEX 3. Bruker Advanced X-ray Solutions, Madison, WI, USA.

Costagliola, P., Benvenuti, M., Tanelli, G., Cortecci, G., Lattanzi, P. (1990): The barite-pyrite-iron oxides deposit of Monte Arsiccio

(Apuane Alps). Geological setting, mineralogy, fluid inclusions, stable isotopes and genesis. *Boll. Soc. Geol. Ital.*, **109**, 267–277.

D'Achiardi, A. (1873): *Mineralogia della Toscana*. Vol **2**. Pisa, Nistri, 404 p.

Del Bucchia, S., Jumas, J.C., Maurin, M. (1981): Contribution à l'étude de composés sulfurés d'étain (II): Affinement de la structure de SnS. *Acta Crystallogr.*, **B37**, 1903–1905.

D'Orazio, M., Biagioni, C., Dini, A., Vezzoni, S. (2017): Thallium-rich pyrite ores from the Apuan Alps, Tuscany, Italy: constraints for their origin and environmental concerns. *Miner. Deposita*, **52**, 687–707.

Engel, P. (1980): Die Kristallstruktur von synthetischem Parapierrotit, $TlSb_5S_8$. *Z. Kristallogr.*, **151**, 203–216.

Engel, P., Gostojić, M., Nowacki, W. (1983): The crystal structure of pierrotite, $Tl_2(Sb,As)_{10}S_{16}$. *Z. Kristallogr.*, **165**, 209–215.

George, L.L., Biagioni, C., D'Orazio, M., Cook, N.J. (2018): Textural and trace element evolution of pyrite during greenschist facies metamorphic recrystallization in the southern Apuan Alps (Tuscany, Italy): influence on the formation of Tl-rich sulfosalt melt. *Ore Geol. Rev.*, **102**, 59–105.

Guillemin, C., Johan, Z., Laforêt, C., Picot, P. (1970): La pierrotite, $Tl_2(Sb,As)_{10}S_{17}$, une nouvelle espèce minérale. *Bull. Soc. Fr. Minéral. Cristallogr.*, **93**, 66–71.

Harris, D.C. (1989): The mineralogy and geochemistry of the Hemlo gold deposit, Ontario. *Geol. Surv. Canada, Econ. Geol. Rep.*, **38**, 88 p.

Johan, Z. & Mantienne, J. (2000): Thallium-rich mineralization at Jas Roux, Hautes-Alpes, France: a complex epithermal sediment-hosted, ore forming system. *J. Czech Geol. Soc.*, **45**, 63–77.

Johan, Z., Picot, P., Hak, J., Kvaček, M. (1975): La parapierrotite, un nouveau minéral thallifère d'Allchar (Yougoslavie). *Tschermaks Mineral. Petr. Mitt.*, **22**, 200–210.

Kabsch, W. (2010): Integration, scaling, space-group assignment and post-refinement. *Acta Crystallogr.*, **D66**, 125–132.

King, N.R. & Richardson, P.D. (2014): The mineral assemblage from Lookout Pass Area, Sheeprock Mountains, Tooele County, Utah. *in* "2014 GSA Annual Meeting in Vancouver, British Columbia".

Lausi, A., Polentarutti, M., Onesti, S., Plaisier, J.R., Busetto, E., Bais, G., Barba, L., Cassetta, A., Campi, G., Lamba, D., Pifferi, A., Mande, S.C., Sarma, D.D., Sharma, S.M., Paolucci, G. (2015): Status of the crystallography beamlines at Elettra. *Eur. Phys. J. Plus*, **130**, 43–51.

Makovicky, E. (1985): The building principles and classification of sulphosalts based on the SnS archetype. *Fortschr. Mineral.*, **63**, 45–89.

— (2018): Modular crystal chemistry of thallium sulfosalts. *Minerals*, **8**, 478.

Makovicky, E. & Topa, D. (2015): Crystal chemical formula for sartorite homologues. *Mineral. Mag.*, **79**, 25–31.

Moëlo, Y., Makovicky, E., Mozgova, N.N., Jambor, J.L., Cook, N., Pring, A., Paar, W.H., Nickel, E.H., Graeser, S., Karup-Møller, S., Balić-Žunić, T., Mumme, W.G., Vurro, F., Topa, D., Bindi, L., Bente, K., Shimizu, M. (2008): Sulfosalt systematics: a review. Report of the sulfosalt sub-committee of the IMA Commission on Ore Mineralogy. *Eur. J. Mineral.*, **20**, 7–46.

Moëlo, Y., Guillot-Deudon, C., Evain, M., Orlandi, P., Biagioni, C. (2012): Comparative modular analysis of two complex sulfosalt structures: sterryite, $Cu(Ag,Cu)_3Pb_{19}(Sb,As)_{22}(As–As)S_{56}$, and parasterryite, $Ag_4Pb_{20}(Sb,As)_{24}S_{58}$. *Acta Crystallogr.*, **B68**, 480–492.

Orlandi, P., Moëlo, Y., Meerschaut, A., Palvadeau, P. (1999): Lead-antimony sulfosalts from Tuscany (Italy). I. Scainiite, $Pb_{14}Sb_{30}S_{54}O_5$, the first Pb-Sb oxy-sulfosalt, from Buca della Vena mine. *Eur. J. Mineral.*, **11**, 949–954.

Orlandi, P., Moëlo, Y., Meerschaut, A., Palvadeau, P. (2001): Lead-antimony sulfosalts from Tuscany (Italy). III. Pillaite, $Pb_9Sb_{10}S_{23}ClO_{0.5}$, a new Pb-Sb oxy-chloro-sulfosalt, from Buca della Vena mine. *Eur. J. Mineral.*, **13**, 605–610.

Orlandi, P., Meerschaut, A., Palvadeau, P., Merlino, S. (2002): Lead-antimony sulfosalts from Tuscany (Italy). V. Definition and crystal structure of moëloite, $Pb_6Sb_6S_{14}(S_3)$, a new mineral from the Ceragiola marble quarry. *Eur. J. Mineral.*, **14**, 599–606.

Orlandi, P., Biagioni, C., Bonaccorsi, E., Moëlo, Y., Paar, W.H. (2012): Lead-antimony sulfosalts from Tuscany (Italy). XII. Boscardinite, $TlPb_4(Sb_7As_2)_{\Sigma 9}S_{18}$, a new mineral species from the Monte Arsiccio mine: occurrence and crystal structure. *Can. Mineral.*, **50**, 235–251.

Orlandi, P., Biagioni, C., Moëlo, Y., Bonaccorsi, E., Paar, W.H. (2013): Lead-antimony sulfosalts from Tuscany (Italy). XIII. Protochabournéite, $\sim Tl_2Pb(Sb_{9-8}As_{1-2})_{\Sigma 10}S_{17}$, from the Monte Arsiccio mine: occurrence, crystal structure and relationship with chabournéite. *Can. Mineral.*, **51**, 475–494.

Plášil, J., Kasatkin, A.V., Škoda, R., Stepanov, S.Y. (2018): Parapierrotite from the Vorontsovskoe gold deposit, Northern Urals, Russia: crystal structure and chemical composition. *Zapiski RMO*, **1**, 68–78.

Raber, T. (2016): Neufunde von der Grube Lengenbach in Binntal: Parapierrotit. *Schweizer Strahler*, **50**, 24–25.

Sheldrick, G.M. (2015): Crystal structure refinement with SHELXL. *Acta Crystallogr.*, **C71**, 3–8.

Wilson, A.J.C. ed. (1992): International tables for X-ray crystallography, Volume C: Mathematical, physical and chemical tables. Kluwer Academic, Dordrecht, NL.